MATERIALS SCIENCE

# Ferroelastic modulation and the Bloch formalism

**Angelo Mascarenhas,* Brian Fluegel, Lekhnath Bhusal**



**The key to the development of advanced materials is to understand their electronic structure-property relationship. Utilization of this understanding to design new electronic materials with desired properties led to modern epitaxial growth approaches for synthesizing artificial lattices, which for almost half a century have become the mainstay of electronic and photonic technologies. In contrast to previous scalar modulation approaches, we now study synthetic crystal lattices that have a tensor artificial modulation and develop a theory for photons and conduction band states in these lattices in a regime with an unusual departure from the familiar consequences of translational symmetry and Bloch's theorem. This study reveals that a nonmagnetic crystal lattice modulated by a purely geometrical orientational superlattice potential can lead to localized states or to spiral states for electrons and photons, as well as weakly or strongly localized states that could be used to markedly slow down the propagation of light and for optical energy storage applications.**

## INTRODUCTION

The band theory of solids (*1*–*7*) forms the foundation for understanding the electrical and optical properties of metals, insulators, and semiconductors based on concepts such as Bloch functions, formation of gaps in the energy spectrum, and the connection between energy surface discontinuities in *k*-space and special points of the Brillouin zone (BZ). Because of the central role played by Bloch's theorem in shaping these concepts, they can be collectively referred to as the Bloch formalism. During the past three decades, this formalism has also provided the framework for developing a band theory of artificially modulated lattices, such as superlattices (*8*) and photonic crystals (*9*). We now report a study on artificially modulated nonmagnetic crystal lattices, whose periodic properties are derived purely by spatial orientation transformations. These orientationally modulated lattices or orientational superlattices (OSLs) have a tensor artificial modulation for which the quantum or wave mechanical description of electrons, photons, phonons, etc., is best accomplished using symmetry transformations for tensors. In contrast to conventional approaches, we demonstrate a regime where a theory for conduction band states can be developed without use of the Bloch formalism, and that the role played by translation symmetry in this development differs from the traditional approach. In addition to propagating states, we observed that a crystalline lattice modulated by a purely geometrical OSL potential can lead to localized states or to spiral states for electrons and photons. The existence of spiral states for electrons and photons in these OSLs is unusual and is associated with the change from Riemann to Finsler geometry (*10*, *11*). We show that for these tensor-modulated structures, the reduction of the space group (*6*) depends on the translation symmetry appropriate for inducing this. The existence of spiral and localized states for electrons and photons can be exploited for electronic, photonic, and optical energy storage applications.

## RESULTS

### Electrons in orientationally modulated lattices

As an example of an OSL, we study a lattice that is constructed out of proper ferroelastic domain wedges with crystalline symmetry $Pmn2_1$ (Fig. 1, inset). The emergence of a ferroelastic spontaneous strain tensor can arise from an order-disorder transition (with a *k*-index of 2 that defines the multiplication of the unit cell) in a material having wurtzite symmetry $P6_3mc$ (*12*, *13*). Periodic twinning of these domains (Fig. 1A) is used to construct the OSL shown in Fig. 1B that is described by the modulated structure space group $P6_3cm$. Because the OSL translation group is a subgroup of the $Pmn2_1$ translation group, the OSL modulation is commensurate. In direct space, the unit cell of the modulated structure (superstructure or superlattice) becomes larger than that of the basic structure and is referred to as a supercell. We explore the theory for conduction band states in these lattices for electrons as well as photons using the effective mass approximation (*14*), wherein the energy eigenfunctions for the bulk domain with symmetry $Pmn2_1$ that constitutes the basic structure are modulated by the OSL periodic potential. We assume a regime where (i) the OSL periodicity is much larger than the period of the $Pmn2_1$ unit cell and (ii) the length of a wedge side, $l \gg \lambda_{de}$, which is the de Broglie wavelength (for light, $\lambda_{\text{in medium}}$). Here, $l$ and $\lambda_{de}$ are large enough that the $6_3$ screw axis or the soft antiphase boundaries (see Materials and Methods) that occur at wedge interfaces can be ignored in the treatment shown below. The difference in the bulk Hamiltonians for any two domain wedges **A** and **B** constituting a domain twin (such as shown in Fig. 1A) is $(\Delta H)_{\mathbf{AB}} = [-V_{\mathbf{A}}(\mathbf{r}) + V_{\mathbf{B}}(\mathbf{r})]$, where $H_{\mathbf{A}} = \frac{\mathbf{p}^2}{2m} + V_{\mathbf{A}}(\mathbf{r})$, $V_{\mathbf{B}}(\mathbf{r}) = RV_{\mathbf{A}}(\mathbf{r})R^{-1}$, and $R$ is the operator that transforms domain wedge **A** into **B**. Let $|\psi^{\mathbf{A}}_{\mathbf{k}}\rangle$ and $|\psi^{\mathbf{B}}_{\mathbf{k}'}\rangle$ correspond to the conduction band eigenstates of $H_{\mathbf{A}}$ and $H_{\mathbf{B}}$, the bulk Hamiltonians for the respective domain wedges. Because $H_{\mathbf{A}}$ and $H_{\mathbf{B}}$ are related by a unitary similarity transformation $R$, they have the same eigenvalues, and the subspace of the one-dimensional (1D) irreducible representation of $H_{\mathbf{A}}$ is one-to-one mapped into that of $H_{\mathbf{B}}$ by $R$ for the corresponding eigenvalues, whereby for conduction band eigenstates of eigenvalue $E$, $|\psi^{\mathbf{A}}_{\mathbf{k}}\rangle \rightarrow |\psi^{\mathbf{B}}_{\mathbf{k}'}\rangle$. Hence, the scattering of a conduction band state of wedge **A** at the interface with wedge **B** by the modulating potential $(\Delta H)_{\mathbf{AB}}$ as it propagates through the OSL is a one-band problem identical to that solved earlier (*15*, *16*). It was shown there that when $R = \sigma$ (the operation for the twin boundary mirror plane transformation), then in the effective mass approximation, for any conduction band state $|\psi^{\mathbf{A}}_{\mathbf{k}}\rangle$ in wedge **A** incident on the twin boundary with bulk wave vector $\mathbf{k}$ corresponding to eigenenergy $E(\mathbf{k})$, there is no back-reflected wave at the twin boundary interface. Thus, for the state $|\psi^{\mathbf{A}}_{\mathbf{k}}\rangle$ propagating in wedge **A**, it is the sequence of refractions at the OSL domain interfaces encountered by this state that determines its propagation through the OSL. Because the refraction rule [for example, as determined by Zhang *et al.* (*15*)] depends only on $\hat{\mathbf{k}} = \mathbf{k}/|\mathbf{k}|$

National Renewable Energy Laboratory, Golden, CO 80401, USA.
*Corresponding author. Email: ajmascar@gmail.com

and not on $|\mathbf{k}|$ or on energy $E(\mathbf{k})$ in the chosen regime, the propagating eigensolutions in the OSL are characterized by $\mathbf{k}$ but are independent of $|\mathbf{k}|$. The irrelevance of $|\mathbf{k}| = 2\pi/\lambda$ for determining the propagating conduction band states is due to the absence of backscattering and resulting destructive/constructive interference generated by the modulating potential. Additionally, in the regime defined above, the conventionally required use of Bloch's theorem is not necessary for determining the propagating eigensolutions in the OSL.

## Photons in orientationally modulated lattices

The similarity between the propagation of light and that of electrons through OSL domain interfaces (*15*) makes it convenient to illustrate the features discussed above, by examining the propagation of light in the *x,y* plane of the OSL (Fig. 1B) when the domain wedges are optically transparent. Light propagation in the OSL birefringent wedges is numerically modeled using section S1 and equation 9 in section S2. A perfectly localized mode and a free mode for a light ray parallel to either the base (a) or the sides (b) of wedges that meet at the center of the hexagonal unit cell are shown in Fig. 2. The OSL domain wedges are chosen to have positive birefringence with values of refractive indices $n_e = (1+\sqrt{2})/\sqrt{3} \cong 1.3938$ and $n_o = 1$ for the extraordinary and ordinary refractions, respectively, and with the wedge length $l \gg \lambda/n_e$ with $\lambda = 0.5$ μm the wavelength of light for this case (a similar localized orbit can be obtained for negative birefringence). The dielectric tensor is of the form given in equation 6 in the study by Zhang *et al.* (*15*). The degree of localization can be varied; for example, if the ray is launched at an angle $\theta = 1.749 \times 10^{-2}$ with the base of the wedge in the hexagon (Fig. 3, top left), the localization is weak, whereas if $\theta = 6.981 \times 10^{-4}$ (Fig. 4, top center), the localization is strong. However, in both cases, the ray now propagates through the lattice. The trajectories in Figs. 2 ( A and B) to 4 categorize the three modes of propagation in the OSL, namely, (i) totally bound, (ii) freely propagating, and (iii) partial resonances, which comprise the vast majority of OSL trajectories. There will be a $2\pi/3$ angular degeneracy in the direction of propagation for trajectories in categories (ii) and (iii). The abovementioned statements apply to a family of parallel rays (see sections S3 and S7).

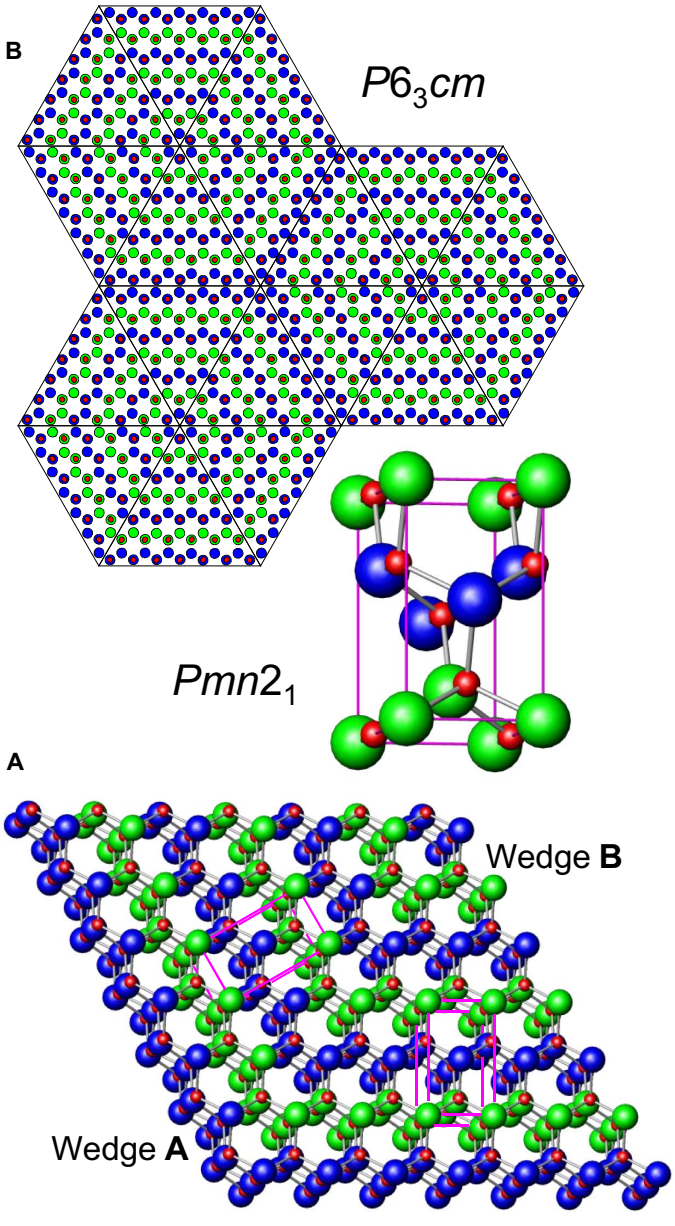


**Fig. 1. Structure of an orientation superlattice.** Bottom: Periodic twinning of domain wedges **A** and **B**, each with crystalline symmetry $Pmn2_1$. Middle: $Pmn2_1$ symmetry unit cell. Top: OSL with symmetry $P6_3cm$.

## Orientationally ordered sublattices

Because of the similarity of the dielectric and effective mass tensor for the birefringent domain wedges [see equations 1 and 6 in the study by Zhang *et al.* (*15*)], the trajectories for ballistic electron states $|\psi_{n\mathbf{k}}\rangle$ with bulk energy $E_n(\mathbf{k})$ in an allowed band with index $n$ of an OSL domain wedge are similar to those for light rays shown in Figs. 2 to 4 (as discussed in section S2). To elucidate the role of translation symmetry in the energy band formalism for the electronic states of the OSL, it is worth noting that the conventional structural ordering of alloys (for example, *R3m*-type ordering in $GaInP_2$) results in a differentiation of sites

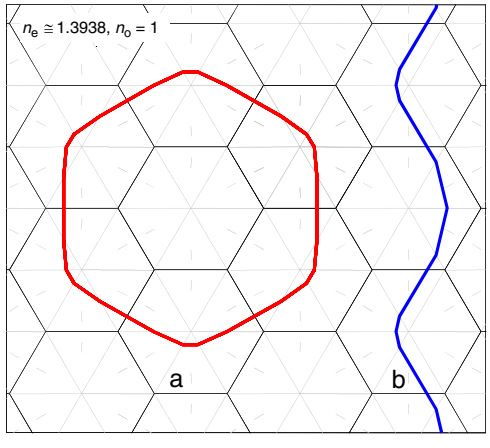


**Fig. 2. Free and localized modes of light.** Perfectly localized and free modes for a ray launched parallel to the base or to the sides of wedges (a) and (b), respectively, that meet at the center of a hexagonal unit cell. Triangular wedge materials are chosen to be positively birefringent, with values of refractive indices $n_e \cong 1.3938$ and $n_o = 1$ for the extraordinary and ordinary refractions, respectively. The direction ⊥ uniaxis is depicted by the tick marks in each wedge. The wedge length $l \gg \lambda$ which is the wavelength of light for this case.

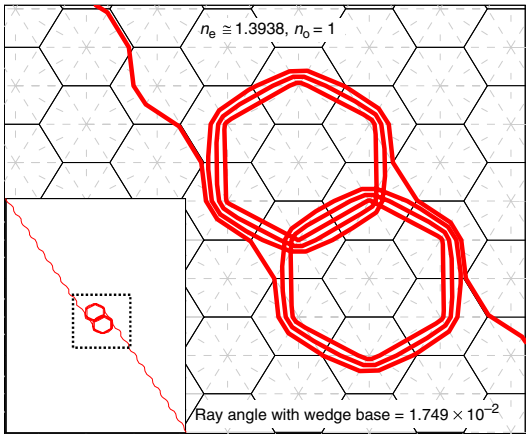


**Fig. 3. Weak localization of light.** Weakly localized mode for a ray launched at an angle of $1.749 \times 10^{-2}$, with the base of the wedge in the hexagon shown at the top left. Inset shows ray propagation on a demagnified scale. The square in the inset is zoomed out in the main figure. The birefringent triangular wedges are identical to those in Fig. 2.

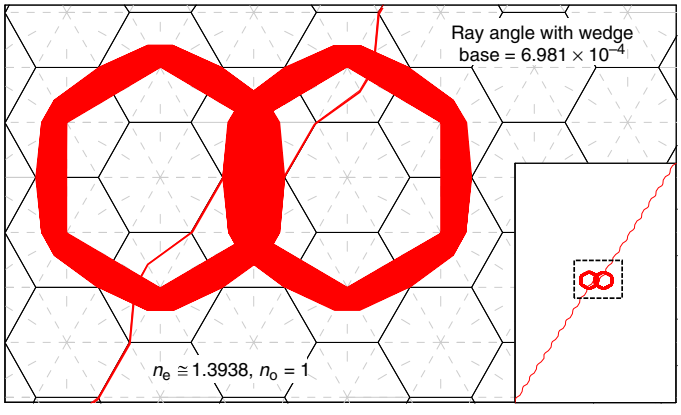


**Fig. 4. Strong localization of light.** Strongly localized mode for a ray launched at an angle of $6.981 \times 10^{-4}$, with the side of the wedge in the hexagon shown at top center. Inset shows ray propagation on a demagnified scale. The square in the inset is zoomed out in the main figure. The birefringent triangular wedges are identical to those in Fig. 2.

on the cation sublattice. Ga and In atoms that occupied the same cation sublattice in $F\bar{4}3m$ $GaInP_2$ now occupy different cation sublattices in $R3m$ $GaInP_2$ (*17*). These differentiated Ga and In sublattices cannot be transformed into one another by a space group operation of the ordered phase $R3m$. The primitive translation that before ordering mapped cations into one another is forbidden subsequent to ordering, and so the translation group gets modified as the size of the direct lattice unit cell gets doubled. In the present situation, the Bravais lattice before orientational ordering is shown in Fig. 5A. Analogous to chemical ordering, "orientational ordering" results in the original Bravais lattice being differentiated into three different sublattices (shown by red, blue, and green dots in Fig. 5B) that cannot be mapped into one another by a space group element of the OSL. The tick marks (which depict the direction $\perp$ uniaxis for wedges) equivalently identify the three orientational sublattices. Thus, in the OSL, the orientational modulation potential introduces a differentiation of the lattice in Fig. 5A into three sublattices. The sublattice space groups $(Pmn2_1)_G$, $(Pmn2_1)_B$, and $(Pmn2_1)_R$ have distinct translation groups $\{\mathbf{t}_G\}$, $\{\mathbf{t}_B\}$, and $\{\mathbf{t}_R\}$, respectively, but they have the same $mm2$ point group. The OSL translation group $\{\mathbf{T}\}$ is an invariant subgroup of $(Pmn2_1)_G$, $(Pmn2_1)_B$, and $(Pmn2_1)_R$ because the sublattice translations $\mathbf{t}$ commute with the OSL translations $\mathbf{T}$.

The conduction band effective mass approximation energy ellipsoids in the $x,y$ plane of the OSL unit cell are shown as shaded ellipses in Fig. 6. Also shown in the figure are how a state with a given wave vector $\mathbf{k}$ in the bulk material of a wedge **A** (blue) when incident on the interface with a wedge **B** (green) gets transformed into a wave vector $\mathbf{k}'$ and, subsequently, how $\mathbf{k}'$ when incident on the interface with a wedge **C** (red) gets transformed into wave vector $\mathbf{k}''$. As shown in the figure, when an electron propagates from one wedge to another, it experiences a reorientation on the new energy ellipsoid. The momenta parallel to the interface are conserved, and so from this value, the refracted electron's momentum normal to the interface can be determined from the new energy ellipsoid. This yields the wave vector refraction rule. The angles of incidence ($\theta_i$) and refraction ($\theta_r$) (see fig. S2) are defined in terms of the current density flow across the interface between wedges **A** and **B** as $\tan(\theta_{i(r)}) = \frac{j_x^{A(B)}}{j_z^{A(B)}}$, yielding the equivalent of Snell's law for the domain twins: $\tan(\theta_r) - \tan(\theta_i) = \frac{2\sqrt{3}(m_\perp - m_\parallel)}{(m_\parallel + 3m_\perp)}$, where $m_\perp$ and $m_\parallel$ are the effective masses $\perp$ and $\parallel$ to the uniaxis, respectively. Replacing current density by power flow yields an analogous equation for photons: $\tan(\theta_r) - \tan(\theta_i) = \frac{2\sqrt{3}(\varepsilon_e - \varepsilon_o)}{(\varepsilon_o + 3\varepsilon_e)}$. Thus, in Fig. 1A, when the conduction band bulk Bloch state $\psi_{\mathbf{k}}(\mathbf{r}) = e^{i\mathbf{k}\cdot\mathbf{r}}u_{\mathbf{k}}(\mathbf{r})$ of a $Pmn2_1$ domain wedge **A** is incident on an interface with wedge **B**, it is transformed into a state $\psi_{\mathbf{k}'}(\mathbf{r}) = e^{i\mathbf{k}'\cdot\mathbf{r}}u_{\mathbf{k}'}(\mathbf{r})$, where $\mathbf{k}$ and $\mathbf{k}'$ are related by the refraction law for the domain twins. Because the refraction is lossless (*15*), the scattering matrix is unitary, and so the transformation of states at the interface can be viewed as a unitary transformation $\mathbf{R_{AB}}|\psi_{\mathbf{k}}\rangle = |\psi_{\mathbf{k}'}\rangle$. The total path length for traveling once around the closed loop in Fig. 2 contributes a spatial phase factor $\delta$ that will be an integral multiple of $2\pi$ if $\delta = \sum_{\text{closed loop}} |\mathbb{k}||\mathbf{r}_d| \cos(\beta) = 2\pi p$, $p = 1,2,3\ldots$, where ($\mathbb{k}$, $\mathbf{r}_d$, $\beta$) vary as the ordered sequence $\{(\mathbf{k}, \mathbf{r_A}, \beta_A), (\mathbf{k}', \mathbf{r_B}, \beta_B), (\mathbf{k}'', \mathbf{r_C}, \beta_C), \ldots.\}$, corresponding to the sequential linear segments of electron propagation in domain wedges **A**, **B**, **C**,….., and where $\beta$ is the angle between the wave vector and the flow of the electron current density. This yields $E = \frac{h^2p^2}{216l^2m_\perp}$, with $k_\perp = \sqrt{\frac{2m_\perp E}{\hbar^2}}$ as the quantization condition for electron-bound states (see sections S6 and S7). As a numerical example of this quantization for the case of light, in a lattice formed of tiles with wedges that have a side length of 2 μm, the bound orbit in Fig. 2 would have quantized energies uniformly separated by 43 meV. In the case of electrons in a tiling of wedges with a side length of 1500 Å and a relative effective mass of 0.1, an electron with an energy of 1.55 eV would result in Fig. 2 having a localized orbit of length = 500 $\lambda_{de}$ and, hence, much smaller separation of the quantized energies.

A spiral orbit is shown in Fig. 7, where the component of $\mathbf{k}$ normal to the OSL $x,y$ plane is chosen to be nonzero ($\mathbf{k}_z \neq 0$). As an example, for closed electron orbits analogous to the positive birefringence OSL in Fig. 2, the anisotropy parameter $\gamma$ is given by $\gamma = \sqrt{m_\perp/m_\parallel} = 1.3938$, which is attainable in practical materials. For example, in the case of fully ordered $GaInP_2$ (order parameter, 1), using the values $m_\perp = 0.2204$ and $m_\parallel = 0.0918$ (here, the conduction band effective mass in the ordering direction is chosen as the value for $m_\perp$) yields $\gamma = 1.5495$, which can be tailored by tuning the order parameter (*15*). The value of optical

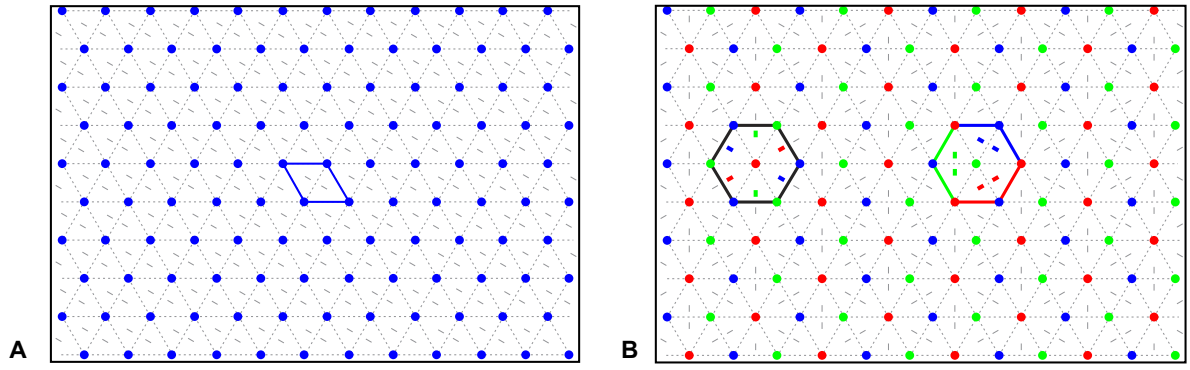


**Fig. 5. Bravais sublattices and orientational ordering.** (**A**) The points in blue denote the Bravais lattice for the $Pmn2_1$-ordered wurtzite structure shown before orientational ordering. The tick marks depict the direction ⊥ uniaxis for wedges, and solid lines depict the unit cell. There will be similar lattices for the other two $Pmn2_1$-ordered variants. (**B**) Orientational ordering of the three ordered variants results in the original wurtzite Bravais lattice being differentiated into three different orientational Bravais sublattices (shown in red, blue, and green, respectively). The tick marks (which depict the direction ⊥ uniaxis for wedges) equivalently identify the three sublattices. The three interpenetrating flat tori for the $P6_3cm$ symmetry OSL lattice are shown to the right of the OSL primitive unit cell.

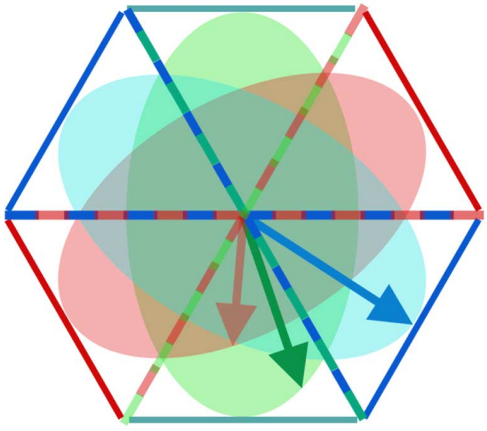

**Fig. 6. Energy ellipsoids and refraction.** Shaded ellipses correspond to effective mass approximation free electron energy ellipses in the *x,y* plane of the $P6_3cm$ symmetry OSL unit cell. The blue vector depicts an electron with a wave vector **k** in a wedge corresponding to a blue sublattice incident on an interface (blue-green line), with a wedge corresponding to a green sublattice. The green vector **k′** depicts the refracted electron. Next, **k′** incident on an interface (green-red line) with a wedge corresponding to a red sublattice gets refracted into the red vector **k″**. The wave vector component along the corresponding interface is preserved at each refraction.

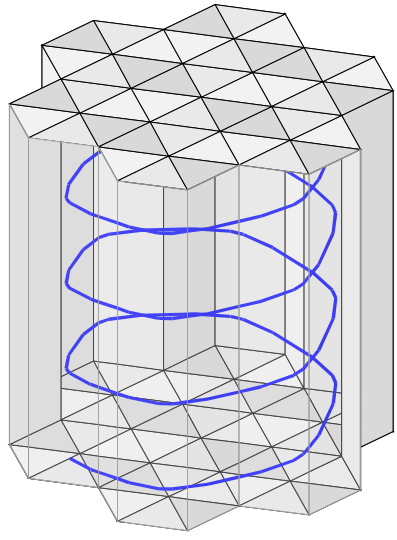

**Fig. 7. Spiral orbit for electrons.** For out-of-plane momentum $k_z \neq 0$, the closed loop trajectory of Fig. 2 evolves into the spiral trajectory for electron propagation in a positive birefringence OSL, with $\gamma = 1.3938$.

birefringence $\Delta n = n_e - n_o$ required to obtain the closed orbits for light in Fig. 2, where $\gamma = n_e/n_o = 1.3938$ is 0.3938, can be obtained using liquid crystals, or photonic crystals where values of birefringence greater than 0.6 are obtainable (*18*, *19*). The techniques used to orient ferroelectric liquid crystals or periodic poling of ferroelectric material can be used for the artificial synthesis of OSLs (*20*, *21*).

## DISCUSSION

In a Landau order-disorder transition, the crystal symmetry transformation from wurtzite $P6_3mc$ to orthorhombic $Pmn2_1$ is associated with a wave vector instability along Σ and subsequent collapse of the wurtzite BZ along this wave vector (see figures S5 and S6 in section S8). The sixfold degeneracy of Σ leads to six possibilities for such a collapse corresponding to six differently oriented $Pmn2_1$ ferroelastic domains (*22*). By neglecting wedge interface defects, the little group $Pmn2_1$ of a wave vector Σ in the OSL is the same as that for wurtzite. Thus, refraction of a conduction band state $\psi_{n\mathbf{k}}(\mathbf{r})$ from one $Pmn2_1$ symmetry ferroelastic domain into $\psi_{n\mathbf{k}'}(\mathbf{r})$ in an adjacent domain corresponds to a change in the description of the state from one little group **k** to another little group **k′**. Although this change of momentum is forbidden in a bulk wurtzite crystal, it becomes allowed in the OSL because of the wedge interface boundaries that give rise to the lossless refraction phenomenon (*15*). The interdomain electron transfer can be described as a transition from one $Pmn2_1$ symmetry BZ (see fig. S6) to another rotated by π/3, just as in Fig. 6. The intradomain transport obeys the translation symmetry of the space group $Pmn2_1$. However, this translation group is not an invariant subgroup of the $P6_3cm$ supergroup corresponding to the OSL because $Pmn2_1$ does not have a sixfold symmetry axis. Thus, **k** changes can occur during interdomain propagation because **k** is not a constant of motion of the OSL. The inter- and intradomain propagation outlined above describes all propagation in the OSL. It is therefore not

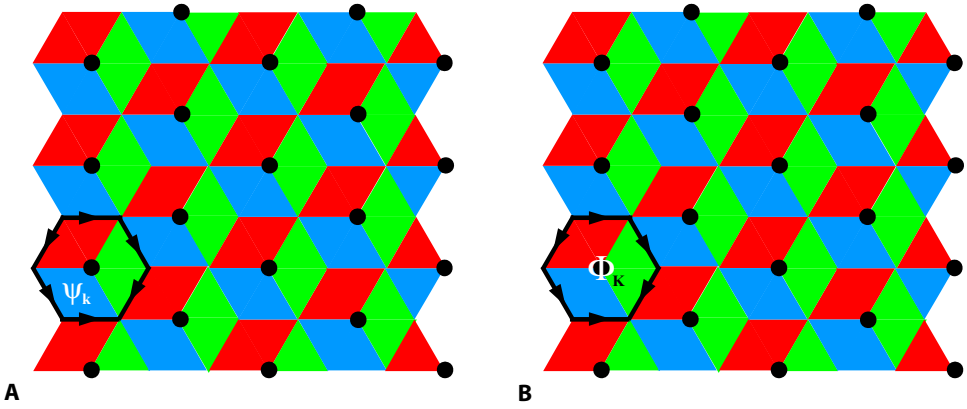


**Fig. 8. Poynting vector (or current density for Bloch states).** (**A**) Bravais lattice for the OSL space group $P6_3cm$, with the outlined plane diagram formed from the hexagonal fundamental domain that was shown at the right of Fig. 5B, is composed of three interpenetrating flat tori. For $l \gg \lambda_{de}$, a Bloch state $\psi_{\mathbf{k}}$ is identified in the blue rhombus with $Pmn2_1$ symmetry domains. Note that **k** changes can occur during interdomain propagation among the red, green, and blue sublattices. (Unlike in Fig. 5B, the sublattice Bravais points are not shown.) The Poynting vector (or current density $\frac{i\hbar}{m^*}\psi^*_{\mathbf{k}}\nabla\psi_{\mathbf{k}}$) for $\psi_{\mathbf{k}}$ will exhibit refraction at the wedge interfaces. (**B**) Bravais lattice for the space group $P6_3cm$ with the hexagonal unit cell outlined in black. For $l \not\gg \lambda_{de}$, a Bloch state $\Phi_{\mathbf{K}}$ derived using the conventional Bloch formalism for the $P6_3cm$ symmetry OSL is identified in the plane diagram. Because **K** is a constant of motion, the Poynting vector (or current density $\frac{i\hbar}{m^*}\phi^*_{\mathbf{K}}\nabla\phi_{\mathbf{K}}$) for $\Phi_{\mathbf{K}}$ yields straight lines (no refraction).

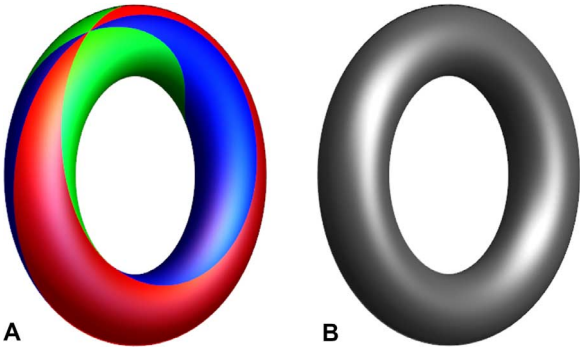


**Fig. 9. Tori representing tricolor and monochromatic Bravais lattices.** (**A**) Torus for tricolor Bravais lattice using the plane diagram shown in Fig. 8A. Here, the translation group of $Pmn2_1$ is used for the reduction of this space group. (**B**) Torus for monochromatic Bravais lattice using the plane diagram in Fig. 8B. Here, the translation group of $P6_3cm$ is used for the reduction of this space group

necessary to invoke the Bloch formalism for the conduction band states of the OSL space group, because although its translation group operations are obeyed by the inter- and intradomain propagation, they were not required in its determination.

The abovementioned Bravais sublattice-to-sublattice propagation mechanism is evident for either the Poynting vector for light or the current density for electrons when a Bloch state $\psi_{n\mathbf{k}}(\mathbf{r})$ in the blue rhombus with $Pmn2_1$ symmetry domains in Fig. 8A refracts into an adjacent red rhombus and then into an adjacent green rhombus, just as they are in Figs. 2 to 4. The hexagonal unit cell of the OSL in Fig. 5B is outlined in black, where the three colors represent the three orientational sublattices. Figure 8B illustrates the procedure of taking the OSL hexagonal unit cell in Fig. 5B, but instead using the conventional Bloch formalism (that is, a single monochromatic Bravais lattice) applicable when condition (i) of the present regime is invalid (that is, where the OSL period is not much larger than the period of the $Pmn2_1$ unit cell). It then does not make sense to describe the individual wedges in terms of states $\psi_{n\mathbf{k}}(\mathbf{r})$ determined using the translation group of $Pmn2_1$ for reduction of this space group (*6*). In this case, the propagation of conduction band states $\phi_{n\mathbf{K}}(\mathbf{r})$ (computed in the conventional Bloch formalism by using the translation group of $P6_3cm$ for reduction of this space group) for the lattice of Fig. 8B results in linear propagation for the Poynting vector or the current density. In this regime, $l \not\gg \lambda_{de}$, and so Bragg scattering effects influence the electronic structure. In contrast, when $l \gg \lambda_{de}$, the size of the OSL BZ becomes trivially small (see figs. S5 and S6), and so Bragg scattering effects are negligible. The difference in the propagation in Fig. 8 (A and B) arises because for the regime in Fig. 8B, OSL Bloch states $\phi_{n\mathbf{K}}(\mathbf{r})$ emerge from the use of a single $P6_3cm$ Bravais lattice with the OSL translation group $\{\mathbf{T}\}$, whereas for the regime in Fig. 8A, the propagation of Bloch states $\psi_{n\mathbf{k}}(\mathbf{r})$ in $Pmn2_1$ symmetry domains recognizes the existence of three orientational Bravais sublattices (see Fig. 9) with translation groups $\{\mathbf{t}_G\}$, $\{\mathbf{t}_B\}$, and $\{\mathbf{t}_R\}$. The unusual existence of spiral states for electrons and photons in these OSLs for the regime discussed in Fig. 8A, in contrast to the regime discussed in Fig. 8B, is associated with the change in the nature of geodesics from Riemann to Finsler geometry (*10*, *11*). The translation group plays a central role in the framework of reduction of space groups, as derived in the study by Seitz (*6*). It appears from Fig. 9 that in the case of tensor-modulated structures, the reduction of space groups depends on the translation symmetry appropriate to induce this in Fig. 8 (A and B).

Although we have used a rudimentary approach to analyze the behavior of photons and electrons in ferroelastic modulated lattices, it satisfactorily explains the data in Figs. 2 to 4. In conclusion, the unusual feature of these lattices for spiraling conduction band electrons without external magnetic fields could be of interest for electronic applications, and the existence of strongly localized and spiral states for photons can be exploited to slow down the propagation as well as for storage of light (*23*, *24*). For the latter, a prism could be used to couple a laser beam into the lattice. This interest could motivate the development of a new generation of the required synthesis techniques (*25*).

## MATERIALS AND METHODS

### Lattice structure and symmetry

The superlattice structure shown in Fig. 1B was designed to have optically perfect interfaces by constructing the tiling out of crystallographic twins

for which the underlying bonding was maintained across every interface. This ferroelastic twinning occurs during an order-disorder transition and is an example of ferroelastic states that emerge across the structural phase transition (*26*). By choosing a parent compound with three equivalent coplanar ordering directions, atomic ordering will ensure both the required birefringence and dislocation-free interfaces shown in Fig. 1. The *k*-index = 2 ferroelastic ordering in wurtzite has three equivalent coplanar directions and produces a point group with refractive index principle directions parallel and normal to the triangular tile base with an ordered orthorhombic $Pmn2_1$ unit cell (Fig. 1A). This could be composed of, for example, ZnS/Se, with S and Se represented by the two large atoms in the figure. The refractive index in the direction normal to the tiling plane would be independent of the indices in the two coplanar directions, and for the purpose of the H-polarization mode exclusively considered here, it may be ignored. For simplicity, we refer to the in-plane principle axis that is parallel to the triangle base as being the optical "uniaxis."

The requirement to form the superlattice using perfect interfaces results in additional constraints on its symmetry group. It is not possible for a triangular wedge formed with a single anion column at its apex to bond to a 60° rotated version of itself. For defect-free bonding, the rotation should be a $6_3$ screw axis that shifts the rotated wedge down one-half lattice constant (Fig. 1). This shift does not affect the macroscopic properties of refractive index or effective mass tensors, and they will maintain a sixfold rotation symmetry. The bonding between the bases of two triangle tiles oriented 180° from each other is more problematic, and to maintain the simple lattice of Fig. 1, it is required that the triangle bases bond at an antiphase boundary. This "soft antiphase" error (it does not involve a cation anion swap) does not affect the principle axis directions and should have a minimal effect on the boundary conditions that determine optical refraction. The final result shown in Fig. 1B has space group $P6_3cm$, which is very similar to that of the original wurtzite structure $P6_3mc$, but differing from it only in the placement of mirror and glide planes relative to the rotation and screw axes. The recent observations of spontaneously generated vortices in ferroelastic materials as well as of self-assembling patterns of six ferroelectric domain states with alternating polarization in hexagonal manganites indicate that there may exist an internal driving force that stabilizes the formation of OSL structures (*27*–*29*).

The effective mass approach used for the treatment of the electronic states is valid in the regime where the OSL periodicity is much larger than the periodicity of $Pmn2_1$ bulk domain potential and where the size of the bulk domains are large enough that the $6_3$ screw axis or the soft antiphase boundaries can be ignored. For example, in a ZnS/Se-based prototypical system, a wedge with 1500 Å side length has approximately $3.1 \times 10^5$ atoms in $3.8 \times 10^4$ unit cells.

### Electronic structure and optical modeling

Light propagation in the OSL birefringent wedges is modeled numerically using equation 9 of section S2, with the electric field in the *x,y* plane. By neglecting interface defects, the OSL point symmetry group *6mm* of the tiling in Fig. 5B is identical to that of the wurtzite tiling. We have ignored scattering at interfaces and at the vertices of the 2D lattice of Fig. 5B because the wedge sizes are assumed to be large, and so the contribution from these effects will be negligible.

## SUPPLEMENTARY MATERIALS

Supplementary material for this article is available at http://advances.sciencemag.org/cgi/content/full/3/6/e1602754/DC1

section S1. Light propagation in anisotropic media
section S2. Electrons in a hexagonal OSL
section S3. Photons in OSLs composed of positive birefringence wedges ($\Delta n = n_e - n_o > 0$)
section S4. The phase-matching condition for photons bound in a given loop
section S5. Photons in OSLs composed of positive birefringence wedges
section S6. Quantization condition for electron bound states
section S7. Electrons in OSLs composed of positive uniaxial wedges
section S8. Direct space and reciprocal lattice with unit cells
fig. S1. Ray and wave normal directions.
fig. S2. Consecutive uniaxial wedges **A** and **B** in the hexagonal unit cell of the OSL.
fig. S3. Photons in OSLs composed of positive birefringence wedges ($\Delta n = n_e - n_o > 0$).
fig. S4. OSL with positive unaxial wedges.
fig. S5. Direct space Bravais lattice and unit cells.
fig. S6. Reciprocal space lattice and unit cells.

## REFERENCES AND NOTES


1. F. Bloch, Über die quantenmechanik der electronen in kristallgittern. *Z. Phys.* **52**, 555–600 (1929).
2. R. E. Peirls, Zur theorie der elektrischen und thermischen leitfähigkeit von metallen. *Ann. Phys.* **396**, 121–148 (1930).
3. P. M. Morse, The quantum mechanics of electrons in crystals. *Phys. Rev.* **35**, 1310–1324 (1930).
4. L. Brillouin, Les electrons libres dans les métaux et le rôle des réflexions de Bragg. *J. Phys. Radium* **1**, 377 (1930).
5. A. H. Wilson, The theory of electronic semi-conductors. *Proc. R. Soc. London Ser. A* **133**, 458 (1931).
6. F. Seitz, On the reduction of space groups. *Ann. Math.* **37**, 17–28 (1936).
7. L. P. Bouckaert, R. Smoluchowski, E. Wigner, Theory of Brillouin zones and symmetry properties of wave functions in crystals. *Phys. Rev.* **50**, 58–67 (1936).
8. L. Esaki, Advances in semiconductor superlattices, quantum wells and heterostructures. *J. Phys. Colloques* **45**, C5-C3–C5-21 (1984).
9. E. Yablonovitch, T. J. Gmitter, Photonic band structure: The face-centered-cubic case. *Phys. Rev. Lett.* **63**, 1950–1953 (1989).
10. S.-S. Chern, Finsler geometry is just Riemannian geometry without the quadratic restriction. *Not. Am. Math. Soc.* **43**, 959–963 (1996).
11. C. Duval, Finsler spinoptics. *Commun. Math. Phys.* **283**, 701–727 (2008).
12. E. K. H. Salje, S. A. Hayward, W. T. Lee, Ferroelastic phase transitions: Structure and microstructure. *Acta Crystallogr. A Found. Adv.* **61**, 3–18 (2005).
13. X. Zhang, D. Chen, K. Deng, R. Lu, Band engineering of wurtzite-derived semiconductors $Cu_2ZnSiS_4$ and $Cu_2ZnSiSe_4$. *J. Alloys Compd.* **656**, 196–199 (2016).
14. P. Voisin, G. Bastard, M. Voos, Optical selection rules in superlattices in the envelope-function approximation. *Phys. Rev. B* **29**, 935–941 (1984).
15. Y. Zhang, B. Fluegel, A. Mascarenhas, Total negative refraction in real crystals for ballistic electrons and light. *Phys. Rev. Lett.* **91**, 157404 (2003).
16. P. F. Schewe, B. Stein, J. Riordon, "Negative and positive refraction at the same crystal interface," in *Physics News in 2003* (American Institute of Physics, 2003); www.aps.org/publications/apsnews/physicsnews/upload/physnews03.pdf.
17. A. Mascarenhas, S. Kurtz, A. Kibbler, J. M. Olson, Polarized band-edge photoluminescence and ordering in $Ga_{0.52}In_{0.48}P$. *Phys. Rev. Lett.* **63**, 2108–2111 (1989).
18. Y. Arakawa, S. Nakajima, S. Kang, M. Shigeta, G.-i. Konishi, J. Watanabe, Design of an extremely high birefringence nematic liquid crystal based on a dinaphthyl-diacetylene mesogen. *J. Mater. Chem.* **22**, 13908–13910 (2012).
19. C.-S. Lee, K. Kim, H. Lim, Tuning of anisotropic optical properties of two-dimensional dielectric photonic crystals. *Physica B Condens. Matter* **338**, 153–158 (2002).
20. P. Ferraro, S. Grilli, P. De Natale, *Ferroelectric Crystals for Photonic Applications* (Springer, 2013).
21. E. K. H. Salje, O. Aktas, X. Ding, Functional topologies in (multi-) ferroics: The ferroelastic template, in *Topological Structures in Ferroic Materials*, Jan Seidel, Ed. (Springer Series in Materials Science, Springer, 2016), pp. 83–101.
22. J. C. Tolédano, P. Tolédano, *The Landau Theory of Phase Transitions: Application to Structural, Incommensurate, Magnetic and Liquid Crystal Systems* (World Scientific, 1987).
23. A. H. Macdonald, P. Schiffer, N. Samarth, Ferromagnetic semiconductors: Moving beyond (Ga, Mn)As. *Nat. Mater.* **4**, 195–202 (2005).
24. T. Baba, Slow light in photonic crystals. *Nat. Photonics* **2**, 465–473 (2008).
25. E. K. H. Salje, Ferroelastic materials. *Annu. Rev. Mater. Res.* **42**, 265–283 (2012).
26. A. Tagantsev, L. E. Cross, J. Fousek, *Domains in Ferroic Crystals and Thin Films* (Springer, 2010).
27. E. K. H. Salje, S. Li, M. Stengel, P. Gumbsch, X. Ding, Flexoelectricity and the polarity of complex ferroelastic twin patterns. *Phys. Rev. B* **94**, 024114 (2016).
28. B. Mettout, P. Tolédano, M. Lilienblum, M. Fiebig, Combinatorial model for the ferroelectric domain-network formation in hexagonal manganites. *Phys. Rev. B* **89**, 024103 (2014).

29. S. M. Griffin, M. Lilienblum, K. T. Delaney, Y. Kumagai, M. Fiebig, N. A. Spaldin, Scaling behavior and beyond equilibrium in the hexagonal manganites. *Phys. Rev. X* **2**, 041022 (2012).

**Acknowledgments**
**Funding:** This work is supported by the Basic Energy Sciences, Division of Material Sciences, under contract no. DE-AC36-08GO28308 with the National Renewable Energy Laboratory.
**Author contributions:** L.B. did the optical modeling; B.F. performed the crystal symmetry and band structure calculations; and A.M. initiated and led the research. **Competing interests:** The authors declare that they have no competing interests. **Data and materials availability:** All data needed to evaluate the conclusions in the paper are present in the paper and/or the Supplementary Materials. Additional data related to this paper may be requested from the authors.

Submitted 7 November 2016
Accepted 7 April 2017
Published 7 June 2017
10.1126/sciadv.1602754

**Citation:** A. Mascarenhas, B. Fluegel, L. Bhusal, Ferroelastic modulation and the Bloch formalism. *Sci. Adv.* **3**, e1602754 (2017).

Science Advances

# Ferroelastic modulation and the Bloch formalism

Angelo Mascarenhas, Brian Fluegel and Lekhnath Bhusal

*Sci Adv* **3** (6), e1602754.
DOI: 10.1126/sciadv.1602754